

An atomistic vision of the Mass Action Law: Prediction of carbon/oxygen defects in silicon

G. Brenet,^{1,2} D. Timerkaeva,^{1,2} E. N. Sgourou,³ C. A. Londos,³ D. Caliste,^{1,2} and P. Pochet^{1,2}

¹CEA, INAC-SP2M, Atomistic Simulation Laboratory, F-38000 Grenoble, France

²Univ. Grenoble Alpes, INAC-SP2M, L_Sim, F-38000 Grenoble, France

³University of Athens, Solid State Physics Section, Panepistimiopolis Zografos, Athens 157 84, Greece

(Received 17 March 2015; accepted 1 September 2015; published online 25 September 2015)

We introduce an atomistic description of the kinetic Mass Action Law to predict concentrations of defects and complexes. We demonstrate in this paper that this approach accurately predicts carbon/oxygen related defect concentrations in silicon upon annealing. The model requires binding and migration energies of the impurities and complexes, here obtained from density functional theory (DFT) calculations. Vacancy-oxygen complex kinetics are studied as a model system during both isochronal and isothermal annealing. Results are in good agreement with experimental data, confirming the success of the methodology. More importantly, it gives access to the sequence of chain reactions by which oxygen and carbon related complexes are created in silicon. Beside the case of silicon, the understanding of such intricate reactions is a key to develop point defect engineering strategies to control defects and thus semiconductor properties. © 2015 AIP Publishing LLC.

[<http://dx.doi.org/10.1063/1.4931569>]

I. INTRODUCTION

Properties in semiconductors are driven by impurity-defect complexes formed during their processing. Several fields of technological interest are impacted by such defect-complexes. In the photovoltaic industry,^{1,2} in fast responding transistor,^{3,4} or in semiconductor lasers,^{5,6} defects have to be controlled or suppressed. The stability and the presence of the latter are often analyzed through the Mass Action Law.⁷⁻⁹ This law states that their binding energy can be used with the Boltzmann statistic to obtain the concentrations. It supposes that the system reaches thermodynamic equilibrium. However, during processing, several interactions compete and thus lead to complex chain reactions. Kinetics controls these kinds of reactions and often leads to metastable situations. The chain reactions cannot be understood only with the defect binding energies. Kinetic Monte Carlo (KMC) simulations could provide such kinetics of formation and dissociation. However, KMC models are computationally expensive and are limited to milliseconds of simulated time at 600 K when fast diffusing species are involved (e.g., mono vacancies in silicon). These limitations can be overcome by working on continuous quantities like concentrations. It corresponds then to a spatial average in the framework of the diffusion-limited reaction theory¹⁰ and of the kinetic Mass Action Law.¹¹

In order to ensure the predictability of such a method, we further introduce an atomistic description for the underlying rate constants. The obtained equations are then solved numerically. Such a simulation tool can handle several dozen of defects and allows to reproduce thousand hours of annealing in a calculation time scale of a minute. In this article, we assess the validity of such an approach on a restricted set of experiments. While few parameters are calibrated on a subset, the whole experimental set is reproduced and found in

very good agreement. In addition, the method gives access to the underlying chain reactions and opens new ways to prevent or select defect formations.

II. THEORETICAL FRAMEWORK

The model is built on the kinetic Mass Action Law.¹¹ It states that in a system with N reactions described by

$$\sum_i \alpha_{ri} A_i \rightleftharpoons \sum_j \gamma_{rj} C_j, r \in \{1, \dots, N\}, \quad (1)$$

the time evolution in concentrations, for one reaction r , is described by

$$\frac{\delta[A_i]_r}{\delta t} = k_{r+} \prod_i [A_i]^{\alpha_{ri}} - k_{r-} \prod_j [C_j]^{\gamma_{rj}}, \quad (2)$$

where $[A_i]$ is the concentration of the reactant i , $[C_j]$ is that of the product j , α_{ri} is the stoichiometric coefficient of reactant i for the forward reaction r , and γ_{rj} is the coefficient of product j in the reaction r . Finally, $k_{r\pm}$ are the rate constants and will be detailed later. In the following, we define that a forward reaction corresponds to the formation of a defect complex and a backward reaction its dissociation.

We use the framework of diffusion-limited reactions. This approximation does not induce a measurable error since the travel time for reactants to meet is much bigger than the time for the reaction to take place. Various models have already been applied in this framework. The most widely used defines the rate constant k_{r+} as $k_{r+} = 4\pi R \times \sum_i D_i$,¹² where $D_i = d_{i0} e^{-\beta E_i^m}$ and R is the capture radius. Nevertheless, there are several disadvantages using this formulation. First, it does not take into account the detailed geometry of the interaction between defects, using instead an isotropic trap

through the capture radius R . The second and main drawback is that the pre-exponential factor d_{i0} in the diffusivity term D_i is expensive to compute as vibrational properties are to be obtained.

Instead, we are defining the rate constant from an atomistic diffusion of a particle, leading to a predictive and more general model. We consider that particles move on a lattice as shown in Fig. 1. In this model, $k_{r\pm}$ can be expressed as follows:

$$k_{r+} = p_0 \times s_i \times \nu_0 e^{-\beta E_r^m} = \frac{p_0 \times s_i}{\langle t_{\text{move}} \rangle}, \quad (3a)$$

$$k_{r-} = \nu_0 e^{-\beta(E_r^m + E_r^b)} = \frac{1}{\langle t_{\text{dissociation}} \rangle}, \quad (3b)$$

where $\nu_0 = 10^{-13} \text{ s}^{-1}$ is the jump frequency, E_r^m is the migration energy of the diffusing particle, and E_r^b is the binding energy between two particles. During a reaction r , we consider only the diffusing species with the lowest migration energy. The other migration rate can be neglected due to the exponential decay in $e^{-\beta E_r^m}$. In Fig. 1, the green species has a higher migration energy. It is thus considered as an immobile defect. The parameter p_0 is an approximate probability for discovering a distinct site, which was never visited before. It depends on the connectivity of the lattice and its type.¹³ In silicon, previous calculations have demonstrated that $p_0 = 0.56$.¹⁴ The factor denoted s_i accounts for the local structure of the defect and its interaction range. A more attractive defect has a higher probability of meeting with other particles. It is defined as the number of neighbor positions for which the binding energy of two separated components is non zero. Thus, this parameter takes into account the capture radius but also the local structure of the defect.

Our approach is based on Eqs. (2) and (3). They give us a system of differential equations. These equations are non-linear in a general case and cannot be solved analytically.

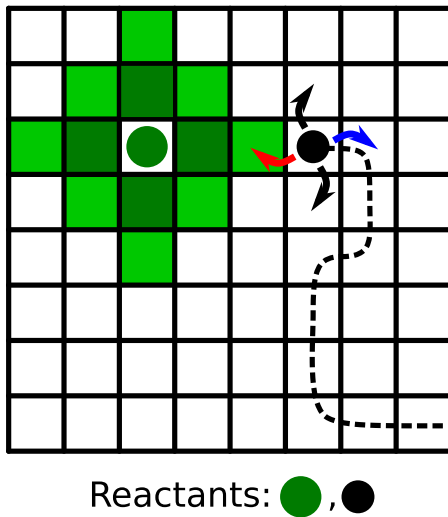


FIG. 1. A representation of a lattice with two species. The green sphere is an immobile trap. The black sphere is a mobile particle. The arrows represent the possible moves. Green squares represent the attractiveness area of the trap. First neighbors are darker than second ones. The dotted line represents the path already crossed by the black particle.

We have solved them numerically using the so-called “Ordinary Differential Equation” solver of Scilab¹⁵ with, respectively, 10^{-12} and 10^{-10} as absolute and relative estimated errors on atomic concentrations. This solver automatically selects between non-stiff predictor-corrector “Adams method” and stiff “Backward Differentiation Formula” method. It uses the non-stiff method initially and dynamically monitors data in order to decide which method to use. It results in a calculation cost of the order of a few minutes for a typical thousand hours simulated annealing time as presented in this paper.

III. CALIBRATION AND ANALYSIS

The model requires three inputs for each reaction: migration and binding energies, and the s_i factor. The binding energies were all calculated using the Density Functional Theory (DFT) approach as in Refs. 16 and 17. We extracted the migration energies also from DFT excepted for the V related complexes. For the latter, we have used experimental values instead due to the known error of the DFT in regard to the excited states at saddle points. The s_i factors, as defined before, are the numbers of neighbors where two separated components have a positive binding energy. They have been calculated by DFT (for the range) and using the connectivity of the silicon lattice. For example, defects on substitutional sites have 4 first neighbors and 12 s neighbors, like carbon related defects; and bond-centered interstitials, like the oxygen, are sitting between 2 substitutional sites, thus having 6 first neighbors. All the corresponding values are listed in Table I.

In the following, we apply our model to reproduce an already published set of experiments^{16,18} where carbon and oxygen react in irradiated silicon. The goal is to first validate our methodology and then analyze the carbon/oxygen related complexes. These experiments consist in successive

TABLE I. Summary of the different reactions and the energy associated in eV. The reactions marked with a star are not considered in the crude simulation Fig. 2(a). s_i is a parameter reproducing the attractiveness of the species. Here, it is the number of first or second neighbors. The binding energies are calculated by DFT or experimentally for those with a reference.

Reaction	Binding energy	Migrating species	Migration energy = forward E_{eff}	$E_b + E_m$ = backward E_{eff}	s_i
$I + C_s \leftrightarrow C_i$	1.45	I	0.40	1.85	4
$2C_i \leftrightarrow C_{i2}$	2.28	C_i	0.58	2.86	4
$C_i + C_s \leftrightarrow C_i C_s$	1.25	C_i	0.58	1.86	4
$C_i + O_i \leftrightarrow C_i O_i$	1.29	C_i	0.58	1.87	6
$I + C_i O_i \leftrightarrow C_i O_i I$	1.09	I	0.40	1.49	1
$C_i I + O_i \leftrightarrow C_i O_i I$		C_{il}		1.49	
$2O_i \leftrightarrow O_{i2}$	0.14	O_i	2.38	2.52	6
$V + O \leftrightarrow VO$	1.5	V	0.45 (Ref. 24)	1.95	6
$VO + O_i \leftrightarrow VO_2$	1.20	VO	1.53 (Ref. 23)	2.67	6
$VO + C_i O_i \leftrightarrow C_s O_{i2}$	2.80	VO	1.53	4.27	6
$VO_2 + C_i \leftrightarrow C_s O_{i2}$	2.89	C_i	0.58	3.47	12
$C_s + O_{i2} \leftrightarrow C_s O_{i2}$	0.73	O_{i2}	1.59	2.32	4
$VO_2 + O_i \rightarrow VO_3^*$		VO_2	1.94 (Ref. 21)		12
$VO_3 + O_i \rightarrow VO_4^*$		VO_3	2.12 (Ref. 21)		12
$C_i + I \leftrightarrow C_i I^*$	1.24	I	0.40	1.64	4
$C_i + VO \rightarrow C_s O_i^*$		C_i	0.58		12

annealing during 20 min from 50 °C to 500 °C with a 10 °C step. Annealing is done on irradiated silicon with different concentrations of carbon. Concentrations are extracted from infra-red absorption measures. The absorption coefficients are not all known, which leads to some unknown species concentrations. Nevertheless, in the simulations, it is required to follow each species in order to have all the reactions and thus the correct kinetics. KMC is not able to simulate such time-scale with so many complexes. The presented approach should be able to handle such a complexity.

We split the experimental process in two steps. First, to reproduce the irradiation process, a source term has been added in the previously defined model, assuming a constant formation of Frenkel pairs. Including this source term, the evolution of the various complex concentrations is simulated at room temperature during 20 min as in the experiments. The irradiation process leaves the sample in a non equilibrium state and thus is a good test for our model. During irradiation, self interstitials are trapped by substitutional carbon (C_s), creating interstitial carbon (C_i). These C_i then diffuse and are further trapped by oxygen (O) or carbon substitutional (C_s), creating, respectively, C_iO_i or C_iC_s . Finally, remaining self interstitials are trapped by C_iO_i . On the vacancy side, the chain reaction is much straightforward as vacancies are directly trapped by oxygen to form VO pairs. Other reactions like the ones implying the creation of aggregates of self interstitials or vacancies are not explicitly taken into account in our reaction list. They will appear nonetheless in an effective term that will be detailed later in the article. The goal of this first step is to find the correct concentrations before annealing and validate the chosen set of reactions. The second step is the isochronal annealing itself. Metastable states are reached during this step and are an additional test for our model. It is worth noticing that no cooling steps have been considered between the anneals. Several species interact during such annealing as shown in Fig. 2(b).

We start by a general overview of the experimental reaction chains. Based on experimental measurements,¹⁶ all defects are related to interstitials and vacancies created

during irradiation. The first set we consider is made of VO , VO_2 for the vacancy related complexes and C_iC_s , C_iO_i , C_iO_iI , and C_sO_{i2} for the interstitial related ones. Experimental evidences, see Fig. 2(b), show that C_iC_s , C_iO_i , and VO are the primary species after irradiation. C_iC_s then dissociates just before C_iO_i around 350 °C. These dissociations lead to the release of C_i . At the same temperature, VO diffuses and forms VO_2 . C_i recombine with VO and VO_2 , forming C_sO_{i2} . This is the final product of the reaction sequence, as experimentally observed. However, most of these reactions happen in the same temperature range. Next, we would like to support the relevance of our atomistic description and investigate the physical meaning of the factors s_i and the parameter p_0 . Thus, we have done a first crude simulation (Fig. 2(a)) that does not take into account the capture radius ($s_i = 1$ for all i) and the probability of visiting the same site twice ($p_0 = 1$). This simulation shows that after irradiation, the ratio between C_iC_s and C_iO_i is not consistent with the experimental ratio.¹⁹ This inconsistency is due to the use of the same capture radius and is corrected by assigning to each species a physical structural parameter (s_i in Table I) allowing to reproduce the specific structure of each trap. In addition, a slight error on the temperatures of the reactions is also visible in Fig. 2(a). This can be corrected by using the proper value for p_0 . Both effects prove the relevance of our atomistic description and that these two parameters are required to predict accurately the concentrations and the transition temperatures. Besides, this first simulation also reveals additional discrepancies with respect to the experimental data due to some missing reactions in the initially considered reaction chain:

- (1) First, the shape of the VO_2 curve in Fig. 2(a) does not reproduce the experimental trend. We observe a complete disappearance above 450 °C. This comes from the too high amount of C_i released from the C_iO_i and C_iC_s dissociations. Indeed, the C_i further migrate and recombine with VO and VO_2 leading to the mentioned VO_2 disappearance and a corresponding overestimation of the C_sO_{i2} concentration. A simple explanation for a limited concentration of C_i in the experimental data lies in the

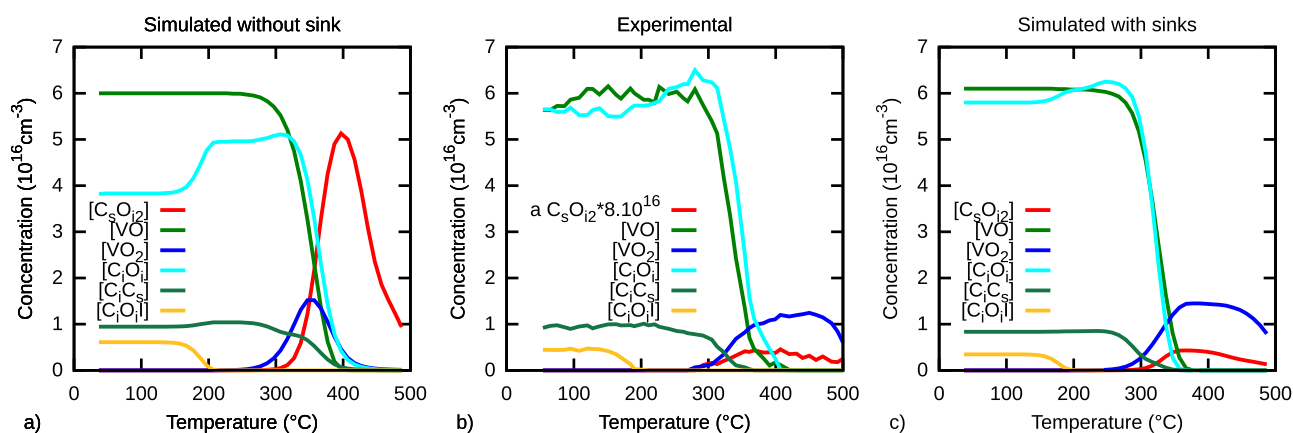


FIG. 2. (a) The simulated concentrations of several species at different temperatures during 20 min annealing with lossless equations. (b) The measured concentrations from experimental data.¹⁶ The absorption curve for the 1048 cm^{-1} band corresponding to C_sO_{i2} species, is labeled “a C_sO_{i2} ”. It has been multiplied by 8×10^{16} to be visible. (c) The numerical results, with losses and the same initial conditions as in (a). The lowest temperature represents the concentrations after irradiation.

trapping of the latter before they reach VO or VO_2 . At the same time, the effect of such sinks is experimentally supported for vacancies. Indeed, in a sample without carbon, there is a 50% loss during the $VO \rightarrow VO_2$ reaction.¹⁸ These sinks can represent various defects, which are neither carbon nor oxygen related ones. They can be structural defects like dislocations, other trapping chemical species, or self clustering. In the following, we have thus added sink terms in the model at an atomic concentration of 7.0×10^{-6} and 5.0×10^{-8} for V/VO and C_i/I , respectively. These two parameters have been calibrated with another set of experiments¹⁸ on samples of equivalent crystalline qualities. The calibrated values for sinks can thus be used for this experiment.

- (2) Second, a quick raise in C_iO_i concentration is visible on Fig. 2(a) at 200 °C, while this raise is slower in experiment. In our simulation, this excess of C_iO_i comes from the dissociation of C_iO_iI into C_iO_i and silicon self interstitials. Thus, one needs to take into account another possible dissociation reaction (i.e., $C_iO_iI \rightarrow C_iI + O_i$) to limit the C_iO_iI concentration. Indeed, as C_iI dissociates at higher temperature, it would allow a slower transition between C_iO_iI and C_iO_i . The existence of C_iI has already been discussed in literature²⁰ and our analysis of the C_iO_i transition further supports its existence.

We now use the full model (Table I) that takes into account all additional reactions and the calibrated sink strength. The simulated kinetics is depicted in Fig. 2(c). It reproduces the main experimental features shown in Fig. 2(b):

- (1) a low raise in C_iO_i concentration between 175 °C and 250 °C, due to the concurrent dissociation of C_iO_iI into C_iO_i on one hand and C_iI on the other hand.
- (2) the C_iC_s dissociation range being in the 270 °C to 320 °C temperature range, as in the experiment. This range comes from a balance between two mechanisms that are required to reproduce the kinetics. The first mechanism is the transfer of C_i to C_iO_i as C_iC_s is less stable than C_iO_i . It is associated with a bump in the C_iO_i concentration just before the C_iO_i dissociation. The second mechanism is the dissociation of both C_iC_s and C_iO_i , which leads to the recombination between V related complexes and C_i as discuss below.
- (3) the transition rate from VO to VO_2 is found to be 1/4 as in the experiment. This reduction can be partially assigned to the presence of C_i . They are stored at low temperature in C_iC_s and C_iO_i complexes. When the complexes dissociate, the C_i are liberated. Then, they recombine with VO and VO_2 to create the C_sO_i and C_sO_{i2} complexes. The latter is experimentally seen (Fig. 2(b)) in the same temperature range as in our simulation with the full model.

IV. PREDICTION OF CARBON/OXYGEN DEFECTS IN SILICON

Next, in order to assess the predictability of our full model (Table I), we have reproduced another set of

experiments.¹⁶ The silicon sample used in the latter experiments has a low content of carbon ($5 \times 10^{16} \text{cm}^{-3}$) and the same amount of oxygen ($9.5 \times 10^{17} \text{cm}^{-3}$). As the samples from both high and low carbon concentrations have the same quality, the same sink concentrations can be used. The results are depicted in Fig. 3. A similar behavior to Fig. 2 is observed. The main transition temperatures are well reproduced, and the evolution in the concentrations is in a good quantitative agreement with the experiments. The main difference between the carbon high sample and the carbon low sample is the C_iC_s concentration. Indeed, due to the low amount of C_s , O_i are now a more efficient trap than C_s . Thus, the C_iO_iI concentration is higher than the C_iC_s . This result appears clearly in the experiment and is perfectly reproduced in our simulation. The phenomena of C_i transfer from C_iC_s and C_iO_iI to C_iO_i are thus confirmed. Significantly, the raise of C_iO_i concentration from $2.8 \times 10^{16} \text{cm}^{-3}$ to $3.3 \times 10^{16} \text{cm}^{-3}$ is well reproduced without any further calibration.

Up to now, the two simulated kinetics are isochronal annealing. Isothermal annealing is also used in the literature²¹ and should be reproducible with our full model and its

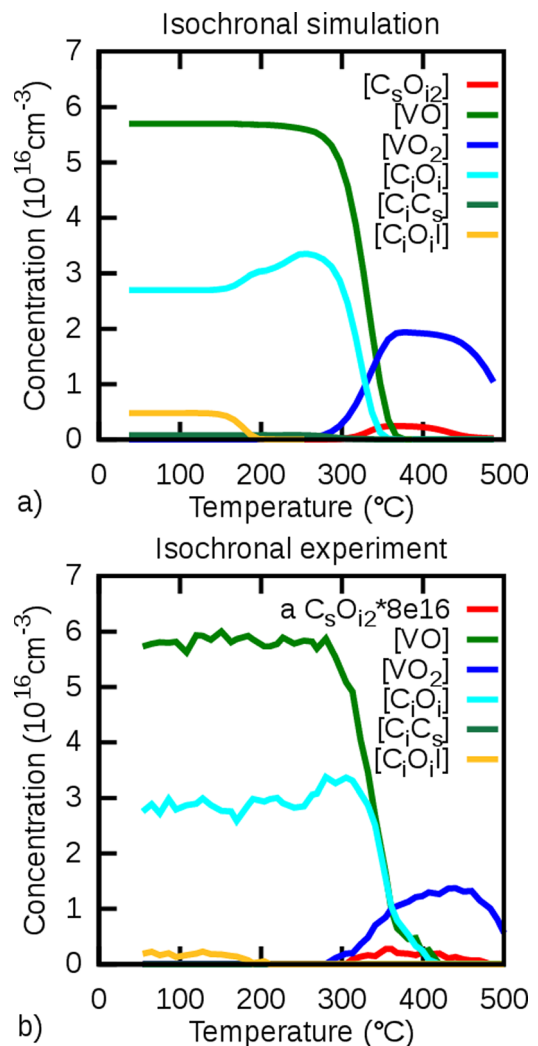


FIG. 3. (a) The simulated concentrations of several species at different temperatures after 20 min annealing taking losses into account. The equations are the same than in Fig. 2 but the initial conditions are different. (b) The measured concentrations from experimental data.¹⁶

calibration. Still we have to introduce the creation of VO_n complexes up to $n \leq 4$ (Table I), as they are detected during the two reported isothermal annealing.²¹ The corresponding silicon sample has an oxygen concentration of $1 \times 10^{18} \text{cm}^{-3}$ and no detectable carbon ($< 5 \times 10^{14} \text{cm}^{-3}$). In addition, there is no experimental sign of a decrease in the vacancy concentration,²¹ and thus we can use the full model without any sinks. The results are presented in Fig. 4 and compared to the experimental data as extracted from figure 3 of Ref. 21. While the agreement is excellent at 370 °C, we observe a slight time shift for 470 °C. We assign this shift to the cooling time of the sample that is not accounted in our simulation. Indeed, the cooling and annealing times are of the same order of magnitude in this latter experiment. Interestingly, the VO behavior is well reproduced despite a difference in the migration energy between our simulation and the experimental analysis.²¹ This difference between the migration energies is indeed balanced by the diffusion constant, which is lower in the simulation. Such effect is well described by the Meyer-Neldel rule.²² Nevertheless, the used energy in the full model is in the line of previous experiments.²³

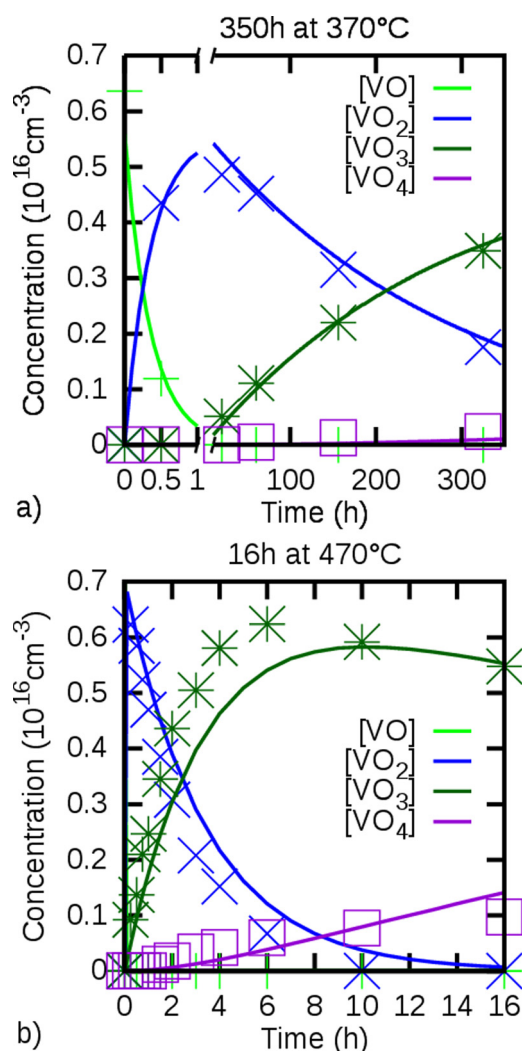


FIG. 4. The figure (a) represents a simulation of a 350 h annealing at 370 °C. The figure (b) represents a simulation of a 16 h annealing at 470 °C. Lines represent the simulation results and the dots are the experimental results from Ref. 21.

Finally, our simulation can also be used to extract infra-red absorption calibration coefficients for uncalibrated complexes as C_sO_{i2} . Indeed, such a calibration coefficient is required to derive the complex concentrations from the infra-red measurements. Our simulated C_sO_{i2} kinetics well reproduce the shape from their experimental counterpart in both Figs. 2 and 3. A value for the calibration coefficient can thus be derived. The values are $7.8 \times 10^{16} \text{cm}^{-2}$ and $8.6 \times 10^{16} \text{cm}^{-2}$ for high and low carbon samples, respectively. Thus, we propose a calibration coefficient of $8 \pm 1 \times 10^{16} \text{cm}^{-2}$ for the C_sO_{i2} complex.

V. CONCLUSIONS

Our simulations of the kinetics of the complex reactions between vacancy, interstitial, oxygen, and carbon related defects allow us assessing a set of reactions. The good agreement in the temperature transitions between experiments and simulation validates our approach in general and the reaction paths of the considered experimental set. For the latter, the effect of carbon on the vacancy oxygen related defects is now clearer and can be used to propose defect engineering strategies. In this particular case, the existence of the C_iI complex is supported and we have confirmed the ability of carbon to store interstitials at low temperatures (up to 350 °C for 20 min annealing).

From a general perspective, the used approach has proven the possibility to simulate thousands hour long annealing for defects in semiconductors. The flexibility of the model allows several types of annealing such as isochronal, isothermal but also aging, and the simulation time-scales easily reach years. This method is built on a DFT energy landscape, and the kinetic Mass Action Law to obtain the concentrations of defects. Experiments are required to calibrate the sink and source terms. Besides, the model described by Eqs. (2) and (3) is general. Through the parameters s_i and p_0 , it is adapted for any crystal structures and point defect geometries. We have shown that it can predict quantitatively defect concentrations in the framework of the diffusion limited reaction.

ACKNOWLEDGMENTS

This work was performed using HPC resources from GENCI-TGCC (Project No. 2014-096107).

- ¹J. Lindroos, Y. Boulfrad, M. Yli-Koski, and H. Savin, *J. Appl. Phys.* **115**, 154902 (2014).
- ²S. M. Kim, S. Chun, S. Bae, S. Park, M. G. Kang, H.-E. Song, Y. Kang, H.-S. Lee, and D. Kim, *Appl. Phys. Lett.* **105**, 083509 (2014).
- ³S. D. Brotherton and P. Bradley, *J. Appl. Phys.* **53**, 5720 (1982).
- ⁴D. P. Tran, T. J. Macdonald, B. Wolfrum, R. Stockmann, T. Nann, A. Offenhuser, and B. Thierry, *Appl. Phys. Lett.* **105**, 231116 (2014).
- ⁵Z. Wang, S. Su, F. C.-C. Ling, W. Anwand, and A. Wagner, *J. Appl. Phys.* **116**, 033508 (2014).
- ⁶K. Appavoo, M. Liu, and M. Y. Sfeir, *Appl. Phys. Lett.* **104**, 133101 (2014).
- ⁷M. J. Powell and S. C. Deane, *Phys. Rev. B* **53**, 10121 (1996).
- ⁸H. Ch. Alt, Y. V. Gomeniuk, F. Bittersberger, A. Kempf, and D. Zemke, *Appl. Phys. Lett.* **87**, 151909 (2005).
- ⁹Y. Shoirakawa and H. Yamada-Kaneta, *J. Appl. Phys.* **80**, 4199 (1996).
- ¹⁰D. Ben-Avraham, M. A. Burschka, and C. R. Doering, *J. Stat. Phys.* **60**, 695 (1990).
- ¹¹F. Horn and R. Jackson, *Arch. Rational. Mech. Anal.* **47**, 81 (1972).
- ¹²T. R. Waite, *Phys. Rev.* **107**, 463 (1957).

- ¹³I. B. Azarov and M. S. Veshchunov, *JETP* **119**, 473 (2014).
- ¹⁴G. Zumofen and A. Blumen, *Chem. Phys. Lett.* **83**, 372 (1981).
- ¹⁵*Modeling and Simulation in SCILAB* edited by S. L. Campbell, J. P. Chancelier, and R. Nikoukhah (Springer, 2006).
- ¹⁶E. N. Sgourou, D. Timerkaeva, C. A. Londos, D. Aliprantis, A. Chroneos, D. Caliste, and P. Pochet, *J. Appl. Phys.* **113**, 113506 (2013); **113**, 239901 (2013) (Erratum).
- ¹⁷D. Timerkaeva, D. Caliste, and P. Pochet, *Appl. Phys. Lett.* **103**, 251909 (2013).
- ¹⁸C. A. Londos, E. N. Sgourou, D. Timerkaeva, A. Chroneos, P. Pochet, and V. V. Emtsev, *J. Appl. Phys.* **114**, 113504 (2013).
- ¹⁹G. Davies and R. C. Newman, *Handb. Semicond.* **3**, 1557 (1994).
- ²⁰A. Mattoni, F. Bernardini, and L. Colombo, *Phys. Rev. B* **66**, 195214 (2002).
- ²¹V. Quemener, B. Raeissi, F. Herklotz, L. I. Murin, E. V. Monakhov, and B. G. Svensson, *Phys. Stat. Solidi B* **251**, 2197–2200 (2014).
- ²²A. Yelon and B. Movaghar, *Phys. Rev. Lett.* **65**, 618 (1990).
- ²³C. A. Londos, N. V. Sarlis, and L. G. Fytros, *Phys. Stat. Solidi A* **163**, 325 (1997).
- ²⁴G. D. Watkins, J. R. Troxell, and A. P. Chatterjee, in *Defects and Radiation Effects in Semiconductors, 1978* edited by J. H. Albany (Institute of Physics, London, 1979), Chap. 1, pp. 1630.